Spatiotemporal evolution of a transient slip event on the San Andreas fault near Parkfield, California

J. R. Murray
U.S. Geological Survey, Menlo Park, California, USA

P. Segall
Department of Geophysics, Stanford University, Stanford, California, USA

Received 28 January 2005; revised 12 May 2005; accepted 20 June 2005; published 14 September 2005.

[1] In 1993 several baselines of the two-color electronic distance meter (EDM) network at Parkfield, California, deviated from their long-term rates, coincident with anomalous observations from nearby strain meters and a creep meter, as well as an increase in microseismicity. Between October 1992 and December 1994, three $M \sim 4.5$ earthquakes occurred beneath Middle Mountain, near the hypocenter of the 1934 and 1966 Parkfield $M6$ events. We analyzed the two-color EDM data using a Kalman-filtering based technique to image the spatiotemporal evolution of slip on the fault at Parkfield between the mid-1980s and 2003. This method accounts for localized random walk motion of the geodetic monuments and a prominent seasonal signal that affects many baselines. We find that a slip rate increase occurred between January 1993 and July 1996 on the upper 8 km of the fault near Middle Mountain. The peak estimated slip rate during this time was 49 mm/yr, which exceeds the long-term geologic rate of ~35 mm/yr. The slip rate evolution appears episodic, with an initial modest increase after the $M4.3$ earthquake and a much larger jump following the shallower $M4.7$ event in December 1994. This temporal correlation between inferred slip and seismicity suggests that the moderate earthquakes triggered the aseismic fault slip. The EDM data cannot resolve whether transient slip propagated across the nucleation zone of the 1934 and 1966 $M6$ Parkfield earthquakes. However, transient slip and its associated stress release in the hypocentral area of previous Parkfield events is consistent with the nucleation of the 2004 $M6$ Parkfield earthquake elsewhere on the fault.

Citation: Murray, J. R., and P. Segall (2005), Spatiotemporal evolution of a transient slip event on the San Andreas fault near Parkfield, California, *J. Geophys. Res.*, *110*, B09407, doi:10.1029/2005JB003651.

1. Introduction

[2] In recent years, spatially and temporally dense observations from continuously recording geodetic networks have revealed a growing number of transient fault slip events. Aseismic slip is of particular interest for several reasons. For instance, it may serve to relieve stress on a fault that would otherwise be released in an earthquake. Transient slip may also transfer stress to other parts of the fault and conceivably lead to a main shock. Moreover, better understanding of stable slip may provide insights into the frictional dynamics of active faults.

[3] Evidence for transient slip events has been found in several locales worldwide, particularly in subduction zone settings. For example, multiple "silent earthquakes" (aseismic slip events in which the slip is too slow to generate seismic signals that are detectable at teleseismic distances) have been inferred from geodetic data in Cascadia, Japan, and southern Mexico [e.g., *Rogers and Dragert*, 2003; *Miyazaki et al.*, 2003; *Ozawa et al.*, 2002; *Yoshioka et al.*, 2004]. Some of these events are associated with postseismic deformation following earthquakes, while others appear to be spontaneous. The duration of the transient events has ranged from several weeks in Cascadia to years in the Tokai region of Japan. The equivalent moment magnitude of inferred slip has exceeded M_w7 in several places. Studies such as these provide mounting evidence that transient processes are not uncommon in subduction zones.

[4] Shallow transient fault slip has long been recognized in strike-slip settings as well, as evidenced by creep meter and strain meter data [e.g., *Gladwin et al.*, 1994; *Linde et al.*, 1996; *Johnston and Linde*, 2002]. These aseismic slip events seem to occur at transition zones between creeping and locked portions of the San Andreas fault. One such transition exists near Parkfield, CA where the fault is characterized by near-surface slip rates approaching 30 mm/yr in the section northwest of Parkfield [*Lisowski and Prescott*, 1981]. The southeastern section, which last ruptured in the 1857 $M8$ Fort Tejon earthquake, is locked. A similar transition occurs at the NW end of the creeping section near San Juan Bautista.

Copyright 2005 by the American Geophysical Union.
0148-0227/05/2005JB003651$09.00

[5] The unfulfilled prediction of a *M*6 Parkfield earthquake in 1988 ±5 years [*Bakun and Lindh*, 1985] focused attention on the seismotectonic processes that regulate the occurrence of moderate earthquakes there. In particular, it is important to determine whether there is evidence for a change in conditions during the 1966–2004 earthquake cycle that would produce the observed delay of the expected *M*6 event. In the early to mid-1990s creep meter, strain meter, and two-color electronic distance meter (EDM) observations deviated from their long-term trends [*Gwyther et al.*, 1996; *Langbein et al.*, 1999; *Nadeau and McEvilly*, 1999; *Gao et al.*, 2000; *Roeloffs*, 2001]. This was accompanied by an overall increase in moment release from microseismicity [*Nadeau and McEvilly*, 1999]. More recently, a concurrent magnetic anomaly has been identified in data from that time period [*Johnston and Mueller*, 2002]. Although the existence of such observations on a variety of instruments suggests a geophysical origin, the interpretation is complicated by the simultaneous occurrence of increased rainfall after several years of drought [*Roeloffs*, 2001].

[6] Perhaps most intriguing is the coincidence of the deformation anomalies with the occurrence of three $M \sim 4.5$ earthquakes between 1992 and 1994, the biggest events at Parkfield since 1966. During the interseismic period, the hypocentral area of the 1966 and 1934 *M*6 earthquakes was largely aseismic and bracketed by two streaks of microseismicity [*Waldhauser et al.*, 2004]. The seismic events of the early 1990s initiated in the deeper of the two streaks and ruptured toward the 1966 hypocenter [*Fletcher and Spudich*, 1998; *Hellweg and Boatwright*, 1999]. Their temporal correlation with the geodetic anomalies suggests a relationship between the moderate earthquakes and aseismic fault slip.

[7] A number of studies [*Gwyther et al.*, 1996; *Langbein et al.*, 1999; *Gao et al.*, 2000] have interpreted the strain meter and two-color EDM data in terms of an increase in slip rate on the San Andreas. A common feature of these is an inferred area of increased slip rate northwest of Carr Hill (Figure 1). The strain meter data seem to require larger and shallower slip rate increases than do the EDM data. The moment release of the transients inferred in these studies is equivalent to that of an M_w4.3–5.5 earthquake. All of these studies, which will be discussed in more detail in section 5.2, relied on forward models or inversions of the data assuming constant deformation rates over fixed time intervals.

[8] In this study we extend these geodetic analyses by estimating the space-time history of fault slip near Parkfield for the time period 1984–2003 from line length measurements. We seek to determine whether the data require transient slip, and if so to estimate its time of onset, duration, location, and spatial extent. Such inferences, as they relate to patterns of microseismicity and moderate earthquakes, can provide insight into the interplay of seismic and aseismic fault slip.

[9] Our analysis utilizes the Kalman filtering-based method termed the "Extended Network Inversion Filter" (ENIF) discussed by *McGuire and Segall* [2003]. This technique is well suited to problems that require separation of a spatially coherent time-varying signal due to fault slip from time series contaminated by local noise sources that are themselves time varying. In the case of the EDM measurements used here, these noise sources include bench mark instability and annual variations most likely due to seasonal wetting and drying of the soil [*Langbein and Johnson*, 1997; *Langbein*, 2004].

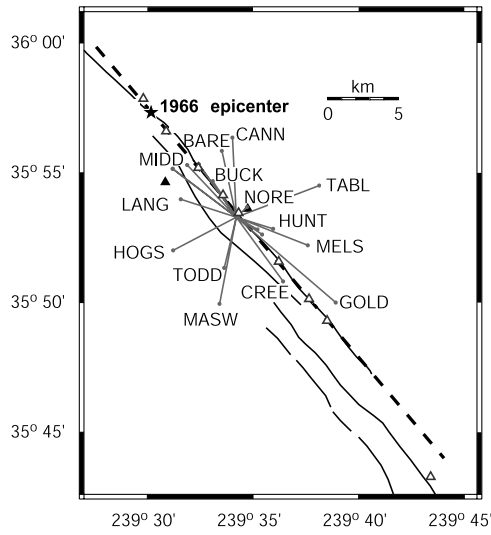

Figure 1. Parkfield permanent two-color EDM network. Central monument (CARR) is at Carr Hill. Solid black lines denote mapped fault trace. Note position of monument MIDD between two mapped traces. Dashed line marks the surface trace of the gridded portion of the model fault plane used in the inversions. Epicenter of the 1966 *M*6 earthquake is shown for reference. Some endpoint bench mark names have been omitted for clarity. Monuments TURK and FLAT are located between the CARR-MELS and CARR-GOLD lines; the CARR-FLAT line is shorter than the CARR-TURK line. Bench mark POMO is located just west of MIDD, and MIDE is located due east of MIDD on the east side of the fault. In 1993, two reflectors were installed with braced monuments which offer improved stability [*Langbein et al.*, 1995]. They are named POMM and MIDA and are collocated with POMO and MIDE, respectively. The locations of creep meters are indicated by open triangles. The two borehole tensor strain meters, FLT and EDT, are shown by solid triangles. FLT is northwest of two-color monument LANG, and EDT is near NORE.

2. Data

[10] The observations used in this study consist of line length measurements from the permanent two-color EDM network at Parkfield [*Langbein et al.*, 1987, 1990]. The core of this network is a laser geodimeter, located at Carr Hill (Figure 1), which modulates signals on both red and blue optical carrier frequencies. Measurements are made to a radial network of retroreflectors surrounding Carr Hill. The network was established in 1984, and measurements were made 2–3 times a week through the 1990s. In 1999 continuous GPS receivers were installed at the sites of five two-color reflectors. Since then, the frequency of two-color observations has decreased as this network is phased out in favor of monitoring with continuous GPS. In mid-2001 nine more GPS stations were installed. Observations of the two-color network have been made one to two times a year since 2003.

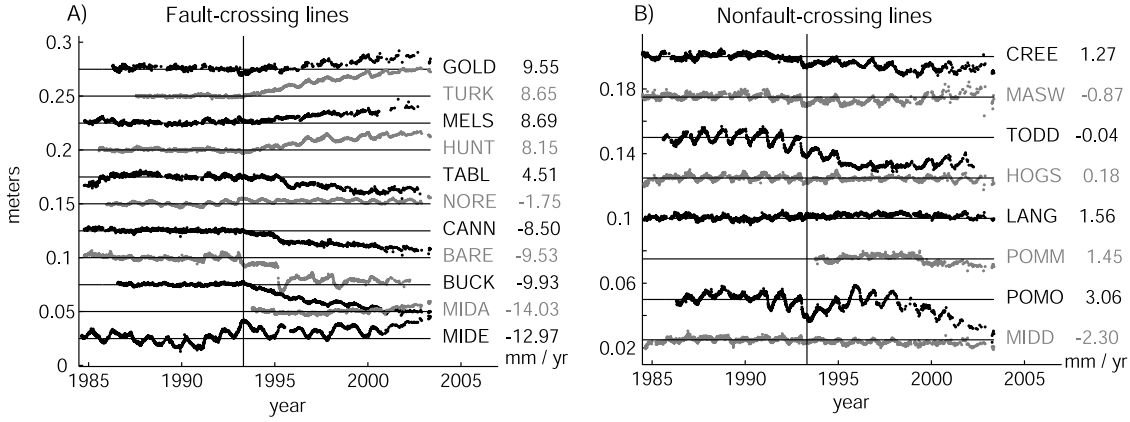

Figure 2. Time series for baselines of the Parkfield permanent two-color EDM network detrended using data up to 26 April 1993 (vertical line). This date was chosen for purposes of display based on visual inspection of the time series. The constant rate (in mm/yr) used to detrend each line is given to the right of the endpoint monument name. Black and gray are used to improve clarity. In August 2000 the permanent two-color EDM instrument at Carr Hill was replaced by a portable instrument, and the observations became less frequent. The scatter in the data increases after this time. The average 1σ measurement errors are 0.5 mm prior to August 2000 and 1.3 mm afterward. (a) Fault-crossing lines; an obvious rate change occurs in April 1993 on several lines. (b) Nonfault-crossing lines.

[11] The time series for the two-color stations are shown in Figure 2. For the purposes of display, a constant rate has been estimated for each baseline using data up to April 1993, and the predicted displacement was removed from the time series. As can be seen (Figure 2), several lines (e.g., BUCK, CANN, HUNT, GOLD, MELS, and TURK) show an apparent rate change in April 1993. Although the onset of this change is fairly distinct and consistent among multiple lines, identifying the point at which the rate returns to its pre-1993 level is more difficult. It is also apparent from Figure 2 that many lines experience strong seasonal variations which need to be accounted for in the analysis. Since the ENIF combines the ability to estimate constant and time-varying displacement due to deformation as well as time-varying noise sources, the raw data (not the detrended data from Figure 2) were used in the analysis.

[12] Line CARR-MIDD (Figure 2) shows displacement inconsistent with nonfault-crossing lines (as evidenced by its pre-1993 rate of −2.3 mm/yr), suggesting that monument MIDD lies in a zone of distributed deformation [*Langbein et al.*, 1990]. Geologic mapping and seismic profiling provide evidence for one or more subparallel fault strands west of the San Andreas in the vicinity of station MIDD [*Rymer et al.*, 2004]. However, the geometry of these structures and their relation to the main trace of the San Andreas, as well as whether they experience interseismic creep, is unclear. Therefore, in our modeling we consider only the main San Andreas fault and omit the CARR-MIDD line from further analysis.

[13] The displacements of the reflector monuments used for these observations are known to exhibit random walk noise to greater or lesser degrees due to minor instabilities of the monuments in the surrounding soil. On average the standard deviation of the random walk is $\sim 0.0013\ \mathrm{m}/\sqrt{yr}$, although some lines are much less stable [*Langbein and Johnson*, 1997; *Langbein*, 2004]. The amplitudes of local seasonal displacements also display a range of behavior both in space and time, and some of the larger deviations are known to be correlated with heavy rainfall (e.g., line BARE in 1995 [*Langbein and Johnson*, 1997]).

3. Modeling

3.1. Extended Network Inversion Filter

[14] The data are modeled using a Kalman filter-based tool referred to as the "Extended Network Inversion Filter" (ENIF) [*Segall and Matthews*, 1997; *McGuire and Segall*, 2003]. Kalman filtering is an efficient means of estimating time-varying processes from noisy data. In the application discussed here the process of interest is fault slip, and the observations are geodetic data. The estimated parameters describing the time-varying process comprise the state vector, $\mathbf{x}$.

[15] The Kalman filter requires two models. The first embodies the time progression of the process of interest. At each epoch the state vector estimated from the previous epoch is used to predict the current value of the model parameters according to this model. In the ENIF, the temporal variation of fault slip is modeled as an integrated random walk process. Slip accelerations are assumed to be a Gaussian white noise process. Therefore integrating the accelerations to obtain the slip rate results in random walk. Integrating again gives slip, which is an integrated random walk process. The local bench mark motion is modeled as a random walk process, consistent with observed spectra of bench mark wobble [*Langbein*, 2004]. Some monuments exhibit both random walk motion and annual signals. We account for the latter as described in section 3.2. The prediction is achieved via the state transition equation

$$\mathbf{x}_k = \mathbf{T}_k \mathbf{x}_{k-1} + \mathbf{w}_k \tag{1}$$

where k is the index of the current epoch and $k-1$ refers to the previous epoch. The matrix $\mathbf{T}$ encompasses the difference equations describing the time progression of the system, which is driven by a noise process, $\mathbf{w}$.

[16] The second required model relates the time-varying process to the data. This may be expressed in the observation equation

$$\mathbf{d}_k = h_k(\mathbf{x}_k) + \epsilon_k \tag{2}$$

where $\mathbf{d}$ are data with errors given by ϵ. The (possibly) nonlinear functions which map the data to modeled processes are given by $h(\mathbf{x})$. Through these relationships, data at a given epoch are used to improve upon the predicted state for that epoch.

[17] As can be seen from equation (1), only the previous epoch's state vector estimate is used in predicting the current state. Furthermore, only the data from the current epoch are used to improve upon the prediction. Therefore new data are efficiently incorporated into the analysis, making Kalman filtering ideal for estimation of an ongoing process.

3.2. Parkfield Transient Deformation Model

[18] The observed changes in line length for the Parkfield two-color EDM network are assumed to contain contributions due to fault slip, random walk bench mark motion, and seasonal signals. A key feature of *Segall and Matthews*' [1997] formulation is that it exploits the spatial coherence of a crustal deformation signal to separate it from random walk noise which is local to each station. Although precleaning the data to remove seasonal variation would reduce the number of estimated quantities, doing so runs the risk of removing a component of the signal that one hopes to model. The observation equation (i.e., equation (2)) used in our analysis is as follows, shown for one baseline:

$$\begin{aligned}(d_k - d_o) = {} & \alpha \mathbf{G}\mathbf{W}_k + \mathbf{G}\dot{\mathbf{s}}_{ss} t + \tau(\beta_k + \beta_{Ck}) \\ & + \eta(A_k + A_{Ck}) \sin(2\pi t/T) + \eta(B_k + B_{Ck}) \\ & \cdot \cos(2\pi t/T) + \epsilon_d, \qquad \epsilon_d \sim N\left(0, \sigma^2 \boldsymbol{\Sigma}_{\mathbf{d}}\right)\end{aligned} \tag{3}$$

[19] The line length data at epoch k relative to a nominal length $(d_k - d_o)$ are assumed to be the sum of contributions from fault slip and noise sources. The formal data covariance is $\Sigma_{\mathbf{d}}$ and is scaled by an estimated factor σ^2.

[20] Fault slip is modeled as a sum of steady state and transient displacement on a dislocation in a homogeneous, linear, elastic half-space. Slip is expressed as $(\dot{\mathbf{s}}_{ss} t + \alpha \mathbf{W})$, where $\dot{\mathbf{s}}_{ss}$ is the steady state slip rate, t is the time elapsed since some reference epoch, and $\mathbf{W}$ is the transient slip modeled as an integrated random walk process with scale parameter α [*Segall and Matthews*, 1997]. Slip is mapped linearly to displacement through the matrix of dislocation Green's functions, $\mathbf{G}$ [e.g., *Okada*, 1985].

[21] Different amounts of random walk and seasonal noise are estimated for each bench mark. The random walk local motion (e.g., bench mark wobble) is represented by β and is scaled by τ in units of m/$\sqrt{\text{yr}}$. The three-component random walk motion of the central (i.e., laser) monument at Carr Hill, β_C is also estimated and projected into each baseline. The seasonal noise is modeled as a sum of sine and cosine terms with time varying amplitudes A and B, where the subscript C refers to seasonal displacement of the central monument projected into the baseline. The period of the seasonal variation, T, is assumed to be one year, although this method may be generalized to model quasi-periodic processes with periods other than a year. The temporal variation of the amplitudes is modeled as a random walk process with scale parameter η.

[22] Following *Harris and Segall* [1987] and *Murray et al.* [2001], the San Andreas near Parkfield is approximated by a 39 km long vertical fault extending from the surface to 14 km depth. The model fault strikes N41°W, and its location is shown by the dashed line in Figure 1. This fault geometry is based on geologic mapping [*Lienkaemper and Brown*, 1985; *Sims*, 1990], the spatial distribution of microseismicity [*Eaton et al.*, 1970; *Eberhart-Phillips and Michael*, 1993], and the inferred rupture area of the 1966 earthquake [*Segall and Du*, 1993]. In order to image spatial variations in fault slip, we discretize the model fault into a grid of uniformly sized blocks (3 km long by 2 km wide). The neighboring creeping and locked sections of the fault are represented by large dislocations (100 km long by 14 km wide) with uniform slip rate. The contribution of motion on the portion of the fault below 14 km, which is assumed to represent deep slip and far-field plate motion, is accommodated by a uniformly slipping dislocation 1000 km long and wide [*Savage*, 1990]. The Green's function relating slip on each subfault to surface displacement is included in the $\mathbf{G}$ matrix. We constrained the slip rate on the creeping section northwest of the Parkfield segment to 25 mm/yr, the approximate value obtained by *Lisowski and Prescott* [1981] for the southern portion of the creeping section. The dislocation below 14 km was constrained to 32 mm/yr, the best fit to the long-term geodetic data [*Murray et al.*, 2001].

[23] There are 10 creep meters spanning the San Andreas in the Parkfield area with data back to the mid-1980s or earlier (Figure 1). Observed creep can provide constraints on near-surface fault slip in the time-dependent inversion. However, as discussed by *Roeloffs* [2001], the data from these instruments exhibit seasonal signals and in some cases show considerable along-strike variation even over short distances. Furthermore, some creep meters may not be long enough to span the entire fault zone, particularly in the vicinity of Middle Mountain (~5 km NW of Carr Hill), and therefore may not record the full near-surface fault creep rate.

[24] The creep meter data were incorporated into the analysis as weak constraints on the slip estimates for the surface-breaking subfaults at each epoch. This was achieved by a one-to-one mapping between the observed creep and slip estimates. The constraints were assigned uncertainties of 1.5 mm. More information on the creep constraints may be found in the auxiliary material[1].

[25] Spatial smoothing was applied to the estimated slip distribution at each epoch using a finite difference Laplacian operator. Purely strike-slip motion was assumed, and positivity constraints were imposed to ensure right lateral slip. Parameters that control the relative weighting of the data (σ) and these constraints (γ for smoothing and ρ for positivity), as well as the temporal variability of the estimated slip (α) and noise sources (τ for bench mark wobble and η for

[1] Auxiliary material is available at ftp://ftp.agu.org/apend/jb/2005JB003651.

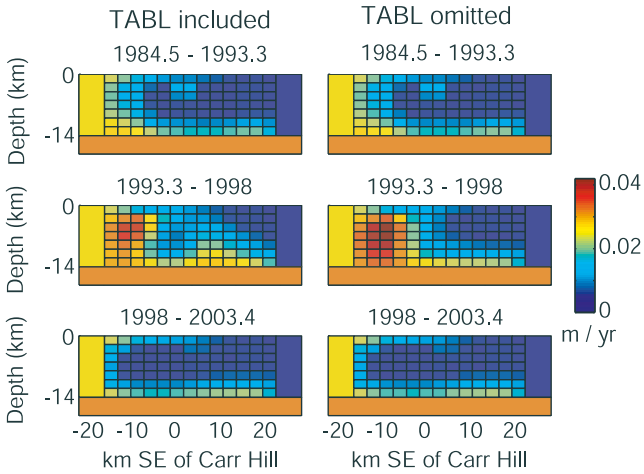

Figure 3. Time-independent inversion for three time periods. Each plot shows the fault plane divided into a grid of subfaults 2 km wide in the downdip direction and 3 km along strike. The larger blocks surrounding the gridded plane are portions of the large, uniformly slipping dislocations which represent the creeping and locked sections of the fault (to the NW and SE, respectively) and the portion of the fault below the transition from seismogenic to nonseismogenic crust. (left) The full two-color data set (with the exception of line MIDD) used in inversions for the spatial distribution of fault slip rate during three time intervals in order to obtain insight into the general patterns of fault slip rate consistent with the data. (right) The time-independent inversions that were repeated with each line omitted in turn to identify which lines had the greatest influence on the solution. Omission of the CARR-TABL line had the biggest effect, as shown here.

seasonal amplitude) are simultaneously estimated by the ENIF during filtering.

4. Results

4.1. Time-Independent Inversion

[26] Prior to conducting the time-dependent inversion we used time-independent inversions to explore the characteristics of slip rate distributions for three subintervals of the observation period: prior to April 1993, April 1993 to the end of 1997, and 1998 to May 2003. We chose these intervals based on the visually apparent rate changes in the two-color EDM data time series. For each time interval a constant rate was fit to the data for each baseline. These rates of line length change were inverted for slip rate as by *Murray et al.* [2001]. Spatial smoothing was imposed using the finite difference approximation of the Laplacian operator. The degree of smoothing was controlled by a parameter which was chosen using tradeoff curves to provide the best combination of spatial smoothness and fit to the data. Observations from creep meter data were used to constrain the slip rates of the surface-breaking subfaults, and a positivity constraint was applied to ensure right-lateral slip rate.

[27] The resulting slip rate distributions (Figure 3, left) were characterized by moderate slip rates (~20 mm/yr) at the northwest end of the fault prior to 1993, higher slip rates (~35 mm/yr) in this location accompanied by elevated slip rate at depth southeast of Carr Hill between early 1993 and late 1997, and very low slip rates over the northwest half of the fault between 1998 and the present. The estimated slip rate distribution for the first time interval is very similar to that found using trilateration data from an earlier time period [*Harris and Segall*, 1987] and to that found using GPS data collected between 1991 and 1998 [*Murray et al.*, 2001]. The shallow high slip rate on the northwestern end of the fault plane during the second time interval and, to a lesser extent, the deeper slip rate increase to the southeast are features also evident in the results of the time-dependent inversions.

[28] In order to assess the influence of each baseline on the imaged slip rate, we repeated these inversions with each baseline omitted in turn. The slip rate distributions were particularly sensitive to the inclusion of data from TABL (compare Figure 3 left and right). Without this line the area of high slip rate on the northwest end of the fault plane extended several kilometers deeper and reached a higher rate during the second time period, while the high slip rate on the deeper part of the fault southeast of Carr Hill was reduced. The line length change predicted by the slip rate distribution obtained with TABL included (Figure 3, left) does not fit the data for the CARR-TABL line (Figure 4). It is evident that the average rate of line length change decreased during the second time interval, while the model predicts a rate increase at TABL. This may be a result of the large offset occurring on this line in 1995, perhaps as a response to heavy rainfall. This baseline is oriented at a high angle to the fault trace, so a large amount of slip is required to produce a small change in line length. Exclusion of this baseline improves the overall fit to the remaining observations. Given the incompatibility of the estimated slip distribution with the observations for the CARR-TABL line and

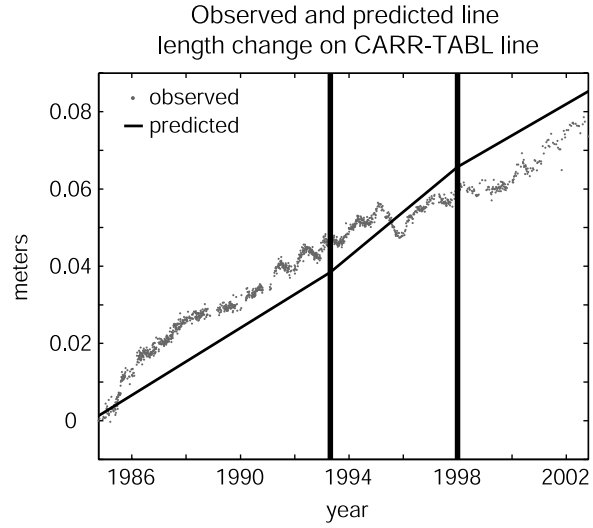

Figure 4. Observed and predicted data for the CARR-TABL baseline. The slip rate distributions shown in Figure 3 (left) were used to predict data for the CARR-TABL baseline (thin black line) during the three time periods (delineated by the vertical black lines). The gray points show the observed line length data. The inferred slip rate distributions give a poor fit to the data for this baseline.

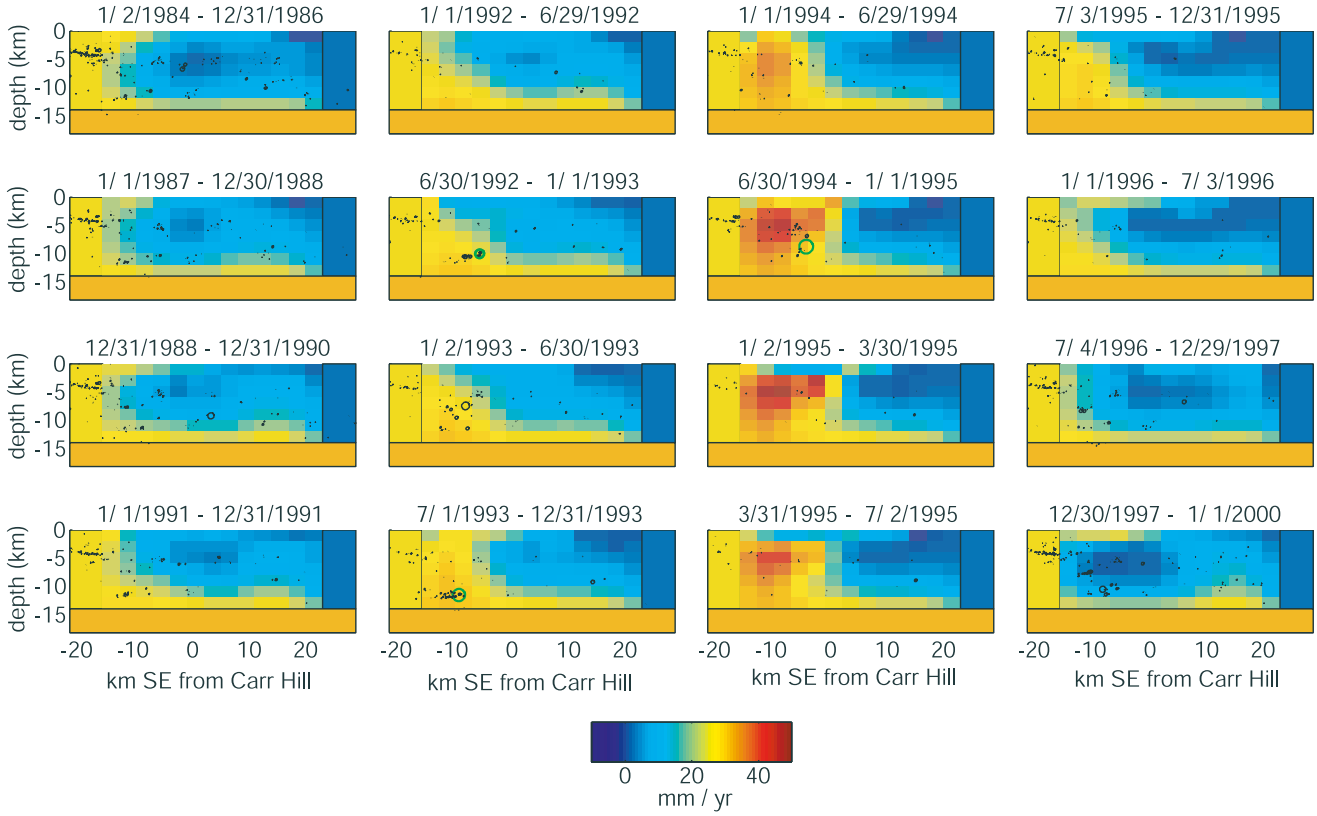

Figure 5. Time history of estimated slip rate distribution. Each panel shows the distribution of slip rate (secular plus transient) at the end of the indicated time interval. Carr Hill (the location of the two-color network's central monument, near the town of Parkfield) is located at zero on the horizontal axis. Superimposed on each panel are the precise relative relocations of microseismicity occurring during the indicated time interval [*Waldhauser et al.*, 2004]. The microseismicity is plotted as the equivalent rupture area of a 3 MPa stress drop crack. The *M*4.3, 20 October 1992, *M*4.6, 14 November 1993, and *M*4.7, 20 December 1994 earthquakes [*Fletcher and Spudich*, 1998] are shown in green. Note area of increased slip rate on the NW end of the fault plane commencing in early 1993.

the potential for this baseline to have strong influence on the slip rate estimates, we have chosen to omit this line in the time-dependent inversions that follow.

4.2. Time-Dependent Inversion Using the ENIF

[29] The results of the time-dependent inversion show a slip rate increase northwest of Carr Hill at a depth of 2–8 km between early 1993 and mid-1996. Figure 5 displays this solution at 16 epochs throughout the observation period. The imaged slip rate history (sum of background steady state rate and transient rate) reaches a maximum of 49 mm/yr in late 1994 to early 1995. As can be seen in Figure 5, the slip rate increase appears to initiate at depths of ~12 km and then move upward, finally concentrating around 6 km depth. However, given the limited power of the EDM data to resolve slip rates on the deeper part of the fault plane, the conclusion that transient slip propagated upward is not robust.

[30] The solution presented in Figure 5 is conditional on all the data (rather than only the observations available up to and including a given epoch) through back smoothing [*Rauch et al.*, 1965]. Although smoothing reduces the model variance, it also obscures rapid changes in slip rate and tends to shift the peak slip rate estimates backward in time. Figure 6 shows the inferred moment rate history for the portions of the fault northwest and southeast of Carr Hill found in the forward run of the filter (i.e., without smoothing).

[31] Between 1992 and 1994 a series of $M > 4$ earthquakes occurred in the vicinity of Middle Mountain. These events (20 October 1992, *M*4.3; 14 November 1993, *M*4.6; and 20 December 1994, *M*4.7) are shown by green circles between −4 and −10 km along strike in Figure 5. The moment rate exhibits a modest increase following the first of these earthquakes (in October 1992) and a dramatic increase after the largest of these events (in December 1994). On the basis of the forward filter slip rate solution, we estimate that the increased slip rate northwest of Carr Hill began with the October 1992 earthquake and lasted until July 1996. The moment released during this time span northwest of Carr Hill was found to be 2.7×10^{17} Nm, equivalent to that of a M_w5.6 earthquake. Tests using simulated data for the Parkfield two-color EDM network verified that the ENIF is capable of detecting an event of this size. On the basis of published slip distributions [*Fletcher and Spudich*, 1998], the predicted surface dis-

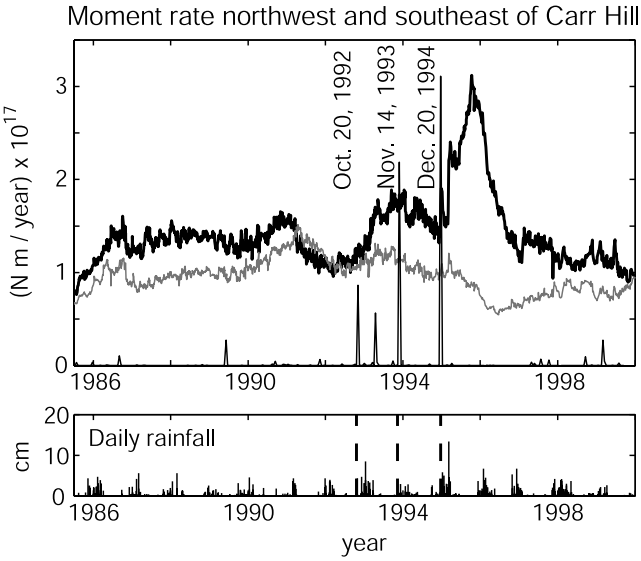

Figure 6. Moment rate history northwest and southeast of Carr Hill. Gray and heavy black curves in Figure 6 (top) show the moment rate from the estimated time-varying slip rate distribution. The solution at each epoch is conditional on data only up to and including that epoch. The heavy black curve is the rate on the northwestmost six columns of subfaults on the model fault plane, and the gray curve is that on the remaining portion of the model fault. The thin black curve shows the moment rate from microseismicity averaged over 15-day windows. The dates of three $M \sim 4.5$ earthquakes are indicated to the left of their corresponding spikes in moment rate. Figure 6 (bottom) shows the daily rainfall for the observation period. Note the increase in rainfall in 1993 and the peak rainfall in 1995. Dashed lines indicate the times of the three earthquakes shown on Figure 6 (top).

placement due to the largest of the three earthquakes does not exceed 1 mm, so the coseismic contribution to the observed EDM signal from these events is negligible.

[32] Data errors and prior variances on the model parameters are propagated through the filter to produce the covariance of the estimated solution. The estimated transient slip rate on individual subfaults (Figure 5) is not significantly different from zero for most of the time period. However, the slip rate estimated at a particular point on the fault is highly correlated with that at neighboring points. Given the model covariance matrix it is possible to obtain rate estimates with lower variance (and correspondingly lower resolution) by spatially averaging the estimated slip rate over multiple subfaults. Figure 7 shows the average slip rate northwest of Carr Hill as a function of time. From this plot it may be seen that the average slip rate between 1994 and 1996 is higher than the background rate on the northwest part of the fault at the 1σ confidence level.

[33] The fit of the solution in Figure 5 to the time series of each baseline is shown in Figures 8 and 9. Both the data and model predictions have been detrended by the observed rate of line length change up to 20 October 1992. The black line in Figure 8 is the signal predicted from the estimated slip history plus the estimated random walk and seasonal noise. In Figure 9 the estimated seasonal noise is removed from

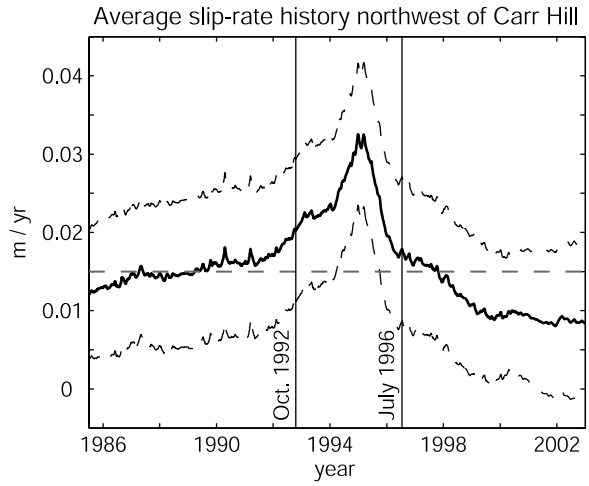

Figure 7. Average slip rate history northwest of Carr Hill. Solid black curve shows the average slip rate on the fault northwest of Carr Hill inferred from the time-dependent inversion. Dashed black curves indicate 1σ errors. Horizontal gray dashed line shows the average pretransient slip rate (15 mm/yr) on this portion of the fault from time-independent inversions (Figure 3, top left). The duration of transient slip inferred from the time-dependent inversion is given by the vertical black lines. The transient increase in slip rate between 1994 and 1996 is significantly higher than the estimated background rate.

the data, and the predicted signal and random walk noise are plotted separately. The seasonal noise model successfully accounts for this noise source, as is shown by the absence of obvious annual trends in the data after removal of the seasonal estimates.

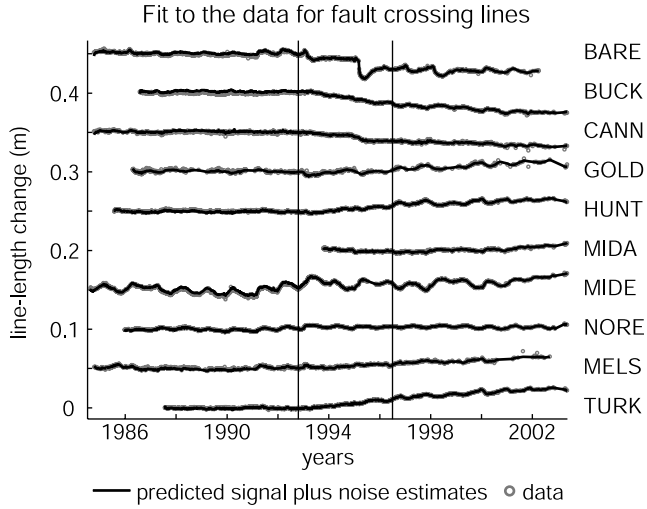

Figure 8. Time series for fault-crossing baselines including observed and estimated seasonal noise. Gray circles are observations and black lines are the data predicted from the estimated slip rate history plus random walk and seasonal noise estimates. Both data and model have been detrended using data up to 20 October 1992. Vertical black lines mark the approximate duration of the imaged slip rate increase. The filter estimates of seasonal noise match the annual fluctuations in the data well.

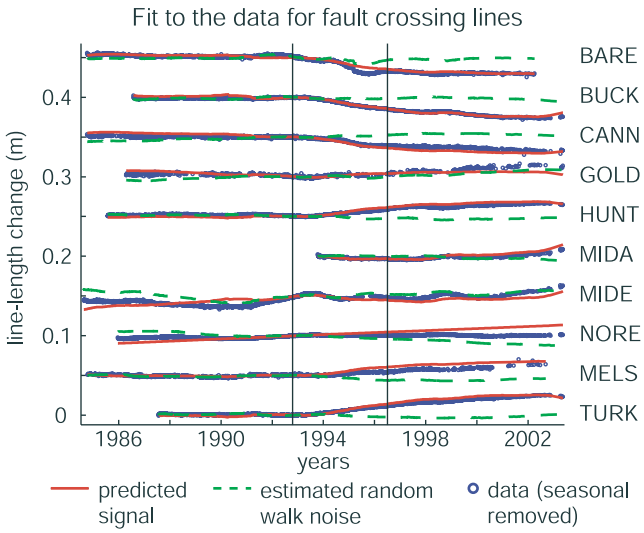

Figure 9. Observed and modeled time series from time dependent inversion for fault-crossing baselines. Blue circles are observations with the estimated seasonal displacement removed; red curves are the line lengths predicted by the estimated slip rate history. Both are detrended using data up to 20 October 1992. The green dashed line shows the estimated random walk local motion. Black lines mark the approximate duration of the imaged slip rate increase.

[34] Assessing whether the predicted line length changes fit the data within the uncertainties in a statistically rigorous way is difficult given the incomplete knowledge of the data errors. The measurements have nominal uncertainties, but the local random walk motion and seasonal noise are estimated as model parameters. We looked for obvious trends in the residuals between the observations and those predicted by the slip model presented in Figure 9. The fit to line NORE was consistently poor, although because this line is short and at a high angle to the fault, the signal-to-noise ratio is low. Line MIDE, which has noticeable temporal variation not fit by the slip model, has been identified by *Langbein et al.* [1990] as potentially unstable. Predicted data for baselines to HUNT, MELS, and TURK appear to slightly overestimate the observed rates during the second half of the transient. Given that the temporal smoothing parameter is estimated during the filter run, this may reflect the time required for the filter to adjust from a higher slip rate at the beginning of the transient to a slightly lower rate after 1995.

5. Discussion

5.1. Comparison With Strain Meter Observations

[35] There are three borehole tensor strain meters (BTSM) and four dilatometers in the Parkfield area for which there are data during the time of the inferred transient deformation. As discussed by *Gao et al.* [2000], the data from two of the dilatometers may be unreliable due to a large annual signal as well as the effects of grout curing and borehole relaxation. Dilatometer data and areal strain measured by the BTSM may be suspect because they are thought to be more strongly influenced by hydrology than shear strain data [*Gwyther et al.*, 1996]. Therefore, given the increased rainfall at Parkfield during the time span of interest, studies of possible transient processes have focused on the shear strains recorded by the tensor strain meters [*Gwyther et al.*, 1996; *Langbein et al.*, 1999; *Gao et al.*, 2000]. Of the three such instruments, data from Donnalee (DLT) shows correlation with rainfall and water well levels, suggesting that these measurements may be contaminated by hydrologic effects [*Gwyther et al.*, 1996].

[36] The remaining two borehole tensor strain meters, Frolich (FLT) and Eades (EDT), exhibited deviations from steady state starting in 1993 [*Gwyther et al.*, 1996]. FLT is located northwest of Carr Hill, 2.4 km from the fault, and EDT is located 0.7 km northeast of Carr Hill near two-color bench mark NORE (Figure 1). The observed strain changes are consistent with increased right lateral slip northwest of these stations (see discussion by *Roeloffs* [2001]).

[37] The strain meter data have not been included in the time-dependent analysis because the reliability of strain meter measurements over periods longer than a few months is not well established, and questions remain regarding the appropriate time-dependent noise model to use for strain data. The application of the ENIF to modeling strain meter data is the subject of ongoing work.

[38] In order to check the consistency of our model with the Parkfield strain observations, we used the estimated transient slip rate history (the slip rate above the background rate over the period January 1993 to July 1996) to predict the two shear strains, $\gamma_1 = \varepsilon_E - \varepsilon_N$ and $\gamma_2 = 2\varepsilon_{EN}$, at FLT and EDT (where E and N refer to east and north, respectively). We then compared these predictions to the observed strain changes published in *Langbein et al.* [1999]. Our findings are presented in Table 1. Our model predicts greater than observed γ_1 at both sites and markedly underpredicts γ_2. The magnitudes of both γ_1 and γ_2 at EDT relative to FLT are generally consistent with the observed changes, and the sign of the predicted strain changes agrees with the observations.

[39] It is evident from this comparison that the strain meter data require even higher slip rate to the northwest of the strain meter sites than we have imaged with the two color EDM data. Other studies have come to a similar conclusion. For instance, *Gao et al.* [2000] considered the direction of maximum extension which can be calculated from γ_1 and γ_2. This orientation is defined by the angle Θ measured counterclockwise from east, where $\tan(2\Theta) = \gamma_2/\gamma_1$. They showed that the direction of maximum extension consistent with the strain meter data, as well as the two-color EDM

Table 1. Predicted and Observed Shear Strain Changes at Two Borehole Tensor Strain Meters Over the Period January 1993 to July 1996

Station	Observed, μstrain	Predicted, μstrain	$\frac{EDT_{obs}}{FLT_{obs}}$	$\frac{EDT_{pred}}{FLT_{pred}}$
		Gamma 1		
EDT	1.94	2.97	2.83	2.37
FLT	0.68	1.25		
		Gamma 2		
EDT	3.19	0.11	−1.04	−1.64
FLT	−3.08	−0.07		

observations, could be reasonably fit by an area of transient slip at a rate of 12 mm/yr NW of Carr Hill in conjunction with transient slip at 3.3 mm/yr reaching the surface below and southeast of Carr Hill. *Gao et al.* [2000] were unable to match the magnitude of the observed strain changes. *Roeloffs* [2001] notes that a threefold increase in the average along-strike slip gradient is needed to generate the observed change in γ_2 strain rate during the transient, and that this is not consistent with observed temporal variations in creep meter data. *Langbein et al.* [1999] conducted a joint inversion of the strain meter and two-color data and, as discussed below, achieved a satisfactory fit to both data sets.

5.2. Comparison With Other Studies

[40] A comparison of our findings with those of other studies that have imaged transient slip rate increases northwest of Carr Hill in the mid-1990s is discussed in section 5.2.

[41] *Gao et al.* [2000] estimated rates of line length change for the two-color network over three time periods. They sought forward models consisting of dislocations with spatially uniform slip rate that fit the rates of line length change estimated for the 1993–1998 time period as well as the direction of maximum extension inferred from the BTSM data. They concluded that two areas of increased slip rate were required, one 10 km long and 9 km wide centered 2 km southeast of Carr Hill with a slip rate change of 3.3 mm/yr and another to the northwest of Carr Hill which was 15 km long, 7 km wide, and had a slip rate increase of 12 mm/yr. Such a transient would have released moment equivalent to that of a M_w5.5 over 5 years. In comparison, for the area spanned by their northwestern dislocation, the average transient slip rate for the 1993–1998 period from our model is 10 mm/yr. For the southern dislocation, the average transient slip rate from our model is 5.5 mm/yr.

[42] *Langbein et al.* [1999] used the two-color EDM data to estimate the secular slip rate for the 1986–1998 period and a rate change between 1993 and 1998. They inverted both the two-color and strain meter data for the spatial distribution of the slip rate change. The transient slip rate they image is characterized by areas of increased slip rate both northwest and southeast of Carr Hill with no rate increase directly below CARR. The slip rate northwest of Carr Hill is required to fit the data, while that southeast of Carr Hill is less well constrained. The peak estimated slip rate change of 8.6 mm/yr occurs at shallow depths ~7 km northwest of Carr Hill. The resulting moment release would be equivalent to that of a M_w5.1 event. The biggest difference between the slip rate distribution found here using the time-dependent inversion and that found by *Langbein et al.* [1999] is that we image increased slip rate deeper on the fault and find no increase in shallow slip rate southeast of Carr Hill. These differences are likely due to two factors: (1) Langbein et al. invert both strain meter and two-color EDM data. They use model subfaults of smaller width near the Earth's surface than those used in this study, thus providing more model parameters for fitting the two data sets. (2) We use creep meter data as constraints on the estimated slip for the surface-breaking subfaults.

[43] Our model agrees least well with that of *Gwyther et al.* [1996]. They explored forward models of fault slip rate increases to fit data from the two borehole tensor strain meters. Their preferred model consists of an area of increased slip rate (20 mm/yr above the background rate) propagating at 3 km/year northward along the San Andreas from 4 km to 1 km depth producing a transient lasting 20 months and releasing moment equivalent to that of a M_w4.3 earthquake. As can be seen from Figure 7, although our modeled slip rates are not significantly different from those of *Gwyther et al.* [1996], only briefly do they exceed ~15 mm/yr above the background rate. Moreover, we image transient slip that extends deeper on the fault plane than did *Gwyther et al.* [1996]. These differences reflect both the higher slip rates apparently required by the strain meter data and the greater depth resolution afforded by the two-color EDM data in comparison to the strain meter observations.

[44] *Nadeau and McEvilly* [1999] used changes in the recurrence times of repeating microseismicity to infer a slip rate increase on the fault near Parkfield between 1993 and 1997. Their imaged rate increase initiates near the site of the October 1992 and November 1993 earthquakes and propagates upward and to the southeast along the fault, finally concentrating above the hypocenter of the December 1994 event. This pattern, as well as their maximum estimated slip rate changes approaching 15 mm/yr, are in qualitative agreement with our findings. Direct comparison between our study and that of *Nadeau and McEvilly* [1999] in terms of estimated deep slip rates and possible slip propagation remains inconclusive because the EDM data only weakly constrain the depth distribution of slip rates. The seismicity data provide superior spatial resolution, but in their conversion from moment rate to slip rate Nadeau and McEvilly assume that all stress at the sites of repeating earthquakes is released in these events. This assumption has been questioned, in part because it requires that the repeating earthquakes have extremely high stress drops [*Beeler et al.*, 2001; *Sammis and Rice*, 2001]. The EDM data provide a more direct measure of fault slip rates. An interesting observation made by *Nadeau and McEvilly* [1999] is that both the rate of microearthquakes and the rate of repeating events in the area from ~4 km southeast to 10 km northwest of the 1966 hypocenter decrease noticeably after 1995, and repeating events ceased in 1997. Our model shows a decrease in slip rate in this area beginning in 1998.

5.3. Effect of Rainfall

[45] Deviations from the long-term trend that appeared in data from a variety of monitoring instruments in the Parkfield area during the early to mid-1990s are compelling evidence for an underlying geophysical origin. The strain meter and two-color laser data show trends that are consistent with an increase in slip rate on the fault northwest of Carr Hill. However, the coincident end of a several year drought brought increased rainfall to the area beginning in the winter of 1993 (Figure 6). The greatest rainfall between 1984 and 1998 occurred in 1995. An unusually heavy rainfall event that year is associated with an offset in the time series for station BARE [*Langbein and Johnson*, 1997]. As can be seen from Figures 8 and 9, the estimated random walk and seasonal noise account well for this local displacement. The data predicted from the fault slip solution

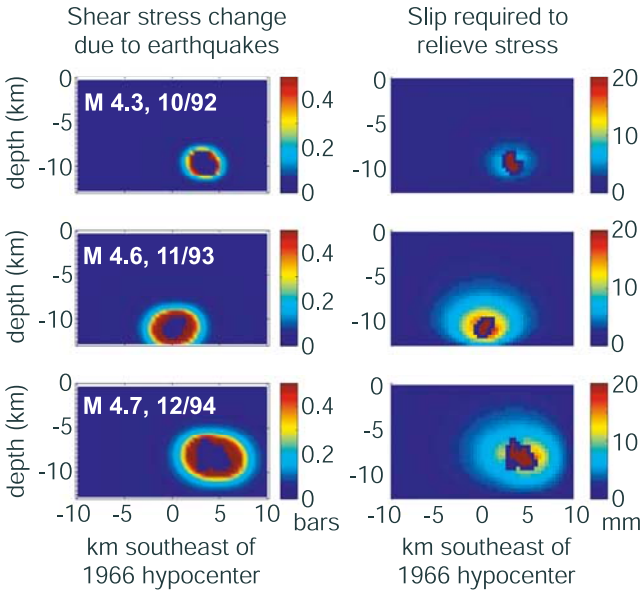

Figure 10. (left) Shear stress changes due to each of three earthquakes calculated from the slip distributions of *Fletcher and Spudich* [1998]. (right) Slip distribution required to relieve the stress changes calculated using the boundary element method. The coseismic rupture areas are shown in red on the plots on Figure 10 (right).

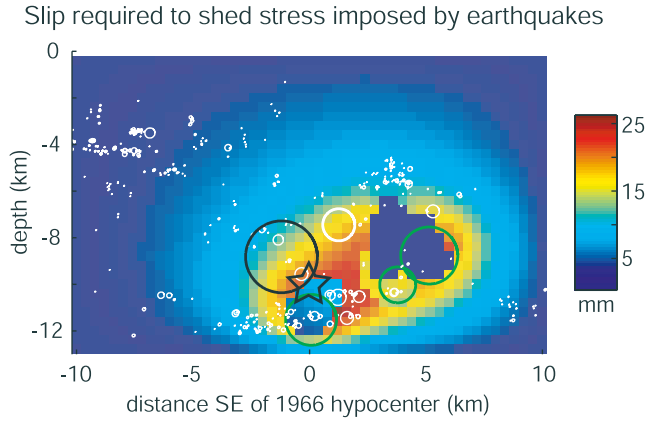

Figure 11. Cumulative slip required to relieve the shear stress increases due to the three $M \sim 4.5$ earthquakes. Superimposed is relocated microseismicity from the time period of the transient [*Waldhauser et al.*, 2004]. The 1966 *M*6 earthquake is shown by the star, and its foreshock is shown by the black circle. The *M*4.3, *M*4.6, and *M*4.7 events are in green. The seismicity is plotted as the equivalent rupture area of a 3 MPa stress drop crack.

alone does not show any sudden offset that would suggest the rainfall-induced displacement maps into the imaged slip history. The transient slip persists in the results of the time-dependent analysis, even with the BARE line omitted. Nevertheless, uncertainty remains in the effect of rainfall on the motion of the shallow monuments and, indirectly, on the fault slip rates [*Roeloffs*, 2001].

5.4. Moderate Earthquakes, Transient Slip, and Stress Changes

[46] The coincidence of the $M \sim 4.5$ events and our inferred slip rate increase lends credence to the idea that the observed two-color rate changes have a geophysical origin. The moment rate evolution (Figure 6) inferred from the forward run of the filter implies that the slip rate increases began following the three earthquakes. This correlation suggests that the earthquakes may have triggered transient slip.

[47] We investigated to what extent the transient slip relieved stress increases on the fault imparted by the three moderate earthquakes. Using the detailed slip distributions obtained by *Fletcher and Spudich* [1998], we calculated the static shear stress change imposed by these events on the fault using expressions given by *Okada* [1992]. We assume that the earthquake ruptures are coplanar with the San Andreas fault, which is consistent with the earthquake relocations given their uncertainties. We calculate the stress changes at the center of each subfault assuming a shear modulus of 30 GPa. The resulting stress distributions are shown in Figure 10. Using the boundary element method, we then calculated the amount of slip on the fault surrounding the coseismic rupture areas that would be required to relieve the stress imposed by each of the three events (Figure 10). To avoid the stress sigularities at the edge of the coseismic rupture, we omitted from the calculations stress changes at points within 500 meters of the rupture area.

[48] The cumulative slip required to relieve the stress changes from all three earthquakes is shown in Figure 11. The moment of this slip is less than 20% that of the cumulative transient slip between 20 October 1992 and 1 July 1996 northwest of Carr Hill shown in Figure 12. The two color EDM observations used in the time-dependent inversion include any signal due to coseismic slip in the three moderate earthquakes. However, the combined moment from these events is small (10–15%) compared to the moment of the inferred transient slip. These findings suggest that the transient event released stored strain on a portion of the fault which experiences steady state creep at about 15 mm/yr. Other studies [e.g., *Hellweg and Boatwright*,

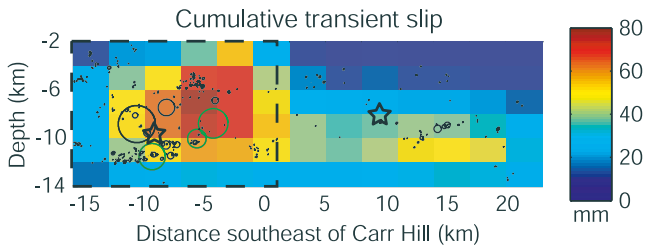

Figure 12. Estimated cumulative transient slip between 20 October 1992 and 1 July 1996 with seismicity during this time period superimposed. The black dashed box indicates the area covered in Figures 10 and 11. Background seismicity (plotted as the equivalent rupture area of a 3 MPa stress drop crack) is shown in black and the three moderate events of the early 1990s in green. The star at about −9 km marks the location of the 1966 hypocenter, and its 17-min foreshock is shown by the largest black circle. The star at ∼8 km is the hypocenter of the 2004 *M*6 earthquake.

1999; P. Johnson and D. Dreger, unpublished manuscript, 1999] have found that the 20 December 1994 earthquake was M_w5 and had a rupture area ~5 km on a side, somewhat larger than that found by *Fletcher and Spudich* [1998]. Repeating the calculations with a greater moment and rupture area for the 1994 event did not change our conclusion; the transient moment was still at least three times that of the required slip. Although slip rates on the northwest portion of the fault are lower after the transient (Figures 5 and 7), the moment rate has not decreased much below the pretransient level (Figure 6). Therefore, by 2003 the posttransient moment deficit northwest of Carr Hill had not compensated for the moment release during the transient.

[49] Superimposed on the slip rate distributions in Figure 5 and the cumulative transient slip distribution shown in Figure 12 are the precise relative relocations of microseismicity. These locations were obtained by *Waldhauser et al.* [2004] using a double-difference algorithm. A notable feature is the presence of subhorizontal streaks of microseismicity, particularly on the northwestern portion of the fault plane. Two such streaks apparently bracket the hypocentral region of the 1966 *M*6 earthquake (Figure 12). The three $M \sim 4.5$ earthquakes of 1992–1994 are indicated by green circles in Figures 5 and 12. As discussed by *Fletcher and Spudich* [1998], these three events nucleated in the deeper of the two streaks and ruptured toward the 1966 hypocenter.

[50] It has been suggested that streaks of microseismicity delineate areas of the fault that are locked [*Waldhauser et al.*, 2004]. It is apparent from Figure 5 that the peak slip rate during the transient concentrates above the shallower of the two streaks of seismicity in the 1966 hypocentral region; the cumulative transient slip in Figure 12 is centered deeper. In the time-dependent inversion it was possible to fit the data when transient slip was, for the length of the streaks, confined either above the upper streak or below the lower streak. However, the latter solution had essentially no transient slip northwest of Carr Hill, in disagreement with strain meter observations.

[51] A model in which the three moderate earthquakes ruptured the lower edge of a locked zone defined by the two streaks in seismicity and caused subsequent transient slip would seem to require, at least for the 1992 and 1993 events, that the transient slip propagated across the region outlined by the streaks. The transient fault slip we have imaged using the EDM data appears to initiate below 8 km depth and propagate upward over time, in keeping with the hypocentral locations of the earthquakes at 9.99 km (1992), 11.58 km (1993), and 8.86 km (1994) [*Fletcher and Spudich*, 1998]. However, given the relatively short baselines (<10 km) of the two-color network, the resolving power for slip on this deeper part of the fault is poor, and therefore such an interpretation must be made with caution.

[52] On 28 September 2004 another *M*6 earthquake occurred at Parkfield [*Langbein et al.*, 2005]. This event, unlike the two previous Parkfield *M*6 earthquakes (and perhaps earlier ones as well), did not nucleate beneath Middle Mountain, but rather at Gold Hill, nearly 20 km to the southeast (Figure 12). The transient slip of the mid-1990s could have promoted another *M*6 earthquake at the 1966 hypocenter if it reloaded that part of the fault. However, the timing and location of the 2004 event suggest the converse. For the transient slip to have inhibited earthquake nucleation beneath Middle Mountain it would have had to reduce stress on the fault, particularly in the 1966 nucleation zone. This would be possible if the transient propagated across the area between the two streaks of seismicity. If transient slip did not propagate across the hypocentral region, it likely increased the shear stress at this location.

[53] According to the rate and state theory of friction, a fault may be characterized by either steady state velocity strengthening or weakening behavior, depending on its frictional properties. Earthquakes nucleate in velocity weakening regions, although slip may propagate into areas of velocity strengthening. As discussed by *Rice and Gu* [1983], transient postseismic slip events may occur in both velocity weakening and velocity strengthening areas. *Marone et al.* [1991] found that observations of shallow afterslip following the 1966 *M*6 earthquake at Parkfield could be fit with a simple model in which the San Andreas above 4 km was assumed to be velocity strengthening and was represented by a one degree of freedom spring slider. In this model, transient slip occurred in response to the stress perturbation caused by arrest of the coseismic rupture as it entered the velocity strengthening region.

[54] *Miyazaki et al.* [2004] conducted time-dependent inversions of GPS data to image afterslip following the 2003 Tokachi-oki earthquake in Japan. They looked at patterns of shear stress on the fault as a function of the natural log of the slip rate and concluded that the inferred slip rate history was consistent with velocity strengthening behavior in the afterslip zone which surrounded the coseismic rupture. We followed their approach using the spatiotemporal history of fault slip at Parkfield. It might be expected that above the upper streak of seismicity at Middle Mountain, where steady creep has been observed for decades, the fault is velocity strengthening. Likewise, areas where earthquakes are known to nucleate, such as within and between the streaks, are presumed to be velocity weakening. However, in examination of the shear stress and slip rate inferred from our time-dependent inversion, no pattern emerged that clearly related frictional behavior and location on the fault. Limited depth resolution on the fault, insufficient frequency of observations directly following the $M \sim 4.5$ earthquakes, and the simplicity of the one degree of freedom model likely all contribute to the inconclusive results regarding fault frictional properties.

6. Conclusions

[55] We have shown that temporal variations in the two-color EDM data at Parkfield are consistent with a transient increase in slip rate on the San Andreas fault northwest of Carr Hill between late 1992 and mid-1996. This analysis accounted for the local effects of bench mark wobble and seasonal noise. The imaged slip rate increase is consistent with that inferred from other studies of two-color EDM data, but less than that inferred from strain meter data. The temporal relation between the imaged slip rate increase and three moderate earthquakes in this region suggests that the seismicity triggered the slip. We infer more slip than that required to dissipate the shear stress increase due to the

three earthquakes, implying that transient slip relaxed stored strain. The peak transient slip rate concentrates above the shallower of two streaks of seismicity which bracket the nucleation zone of the 1966 *M*6 earthquake. We cannot resolve whether transient slip propagated across the hypocentral region of the 1966 *M*6 earthquake. However, the nucleation of the 2004 Parkfield *M*6 earthquake beneath Gold Hill rather than Middle Mountain is consistent with a reduction of stress in the hypocentral zone of the 1934 and 1966 earthquakes, perhaps due to transient slip.

[56] **Acknowledgments.** The authors wish to thank John Langbein, Jim Savage, Wayne Thatcher, and Sang-Ho Yun for valuable discussions and comments on this work. We also wish to thank Roland Bürgmann and an anonymous reviewer for their suggestions for ways to improve the manuscript. This work was funded by a U.S. Geological Survey National Earthquake Hazards Reduction Program grant.

References

Bakun, W. H., and A. G. Lindh (1985), The Parkfield, California earthquake prediction experiment, *Science*, *229*, 619–624.

Beeler, N. M., D. L. Lockner, and S. H. Hickman (2001), A simple stick-slip and creep-slip model for repeating earthquakes and its implication for microearthquakes at Parkfield, *Bull. Seismol. Soc. Am.*, *91*, 1797–1804.

Eaton, J. P., M. E. O'Neill, and J. N. Murdock (1970), Aftershocks of the 1966 Parkfield-Cholame, California, earthquake: A detailed study, *Bull. Seismol. Soc. Am.*, *60*, 1151–1197.

Eberhart-Phillips, D., and A. J. Michael (1993), Three-dimensional velocity structure, seismicity, and fault structure in the Parkfield region, central California, *J. Geophys. Res.*, *98*, 15,737–15,758.

Fletcher, J. B., and P. Spudich (1998), Rupture characteristics of the three $M \sim 4.7$ (1992–1994) Parkfield earthquakes, *J. Geophys. Res.*, *103*, 835–854.

Gao, S., P. G. Silver, and A. T. Linde (2000), A comprehensive analysis of deformation data at Parkfield, California: Detection of a long-term strain transient, *J. Geophys. Res.*, *105*, 2955–2967.

Gladwin, M., R. Gwyther, R. Hart, and K. Breckenridge (1994), Measurements of the strain field associated with episodic creep events on the San Andreas fault near San Juan Bautista, California, *J. Geophys. Res.*, *99*, 4559–4565.

Gwyther, R. L., M. T. Gladwin, M. Mee, and R. H. G. Hart (1996), Anomalous shear strain at Parkfield during 1993–94, *Geophys. Res. Lett.*, *23*, 2425–2428.

Harris, R., and P. Segall (1987), Detection of a locked zone at depth on the Parkfield, California, segment of the San Andreas fault, *J. Geophys. Res.*, *92*, 7945–7962.

Hellweg, M., and J. Boatwright (1999), Mapping the rupture process of moderate earthquakes by inverting accelerograms, *J. Geophys. Res.*, *104*, 7319–7328.

Johnston, M., and A. Linde (2002), Implications of crustal strain during conventional, slow, and silent earthquakes, in *International Handbook of Earthquake and Engineering Seismology, Part A*, *Int. Geophys. Ser.*, vol. 81, edited by W. H. K. Lee et al., pp. 589–605, Elsevier, New York.

Johnston, M., and R. Mueller (2002), Tectonomagnetic anomaly observed at Parkfield, CA from 1993 to the present: Correspondence to increased shear strain-rate during the same period, *Eos Trans. AGU*, *83*(47), Fall Meet. Suppl., Abstract G12C-05.

Langbein, J. (2004), Noise in two-color electronic distance meter measurements revisited, *J. Geophys. Res.*, *109*, B04406, doi:10.1029/2003JB002819.

Langbein, J., and H. Johnson (1997), Correlated errors in geodetic time series: Implications for time-dependent deformation, *J. Geophys. Res.*, *102*, 591–603.

Langbein, J., M. Linker, A. McGarr, and L. Slater (1987), Precision of two-color geodimeter measurements: Results from 15 months of observations, *J. Geophys. Res.*, *92*, 11,644–11,656.

Langbein, J., R. Burford, and L. Slater (1990), Variations in fault slip and strain accumulation at Parkfield, California: Initial results using two-color geodimeter measurements, 1984–1988, *J. Geophys. Res.*, *95*, 2533–2552.

Langbein, J., F. Wyatt, H. Johnson, D. Hamman, and P. Zimmer (1995), Improved stability of a deeply anchored geodetic monument for deformation monitoring, *Geophys. Res. Lett.*, *22*, 3533–3536.

Langbein, J., R. L. Gwyther, R. H. G. Hart, and M. T. Gladwin (1999), Slip-rate increase at Parkfield in 1993 detected by high-precision EDM and borehole tensor strainmeters, *Geophys. Res. Lett.*, *26*, 2529–2532.

Langbein, J., et al. (2005), Preliminary report on the 28 September 2004, *M*6.0 Parkfield, California, earthquake, *Seismol. Res. Lett.*, *76*, 1–17.

Lienkaemper, J. J., and R. D. Brown (1985), Map of faulting accompanying the 1966 Parkfield, California, earthquake, *U.S. Geol. Surv. Open File Rep., 85-661*.

Linde, A., M. Gladwin, M. Johnston, R. Gwyther, and R. Bilham (1996), A slow earthquake sequence on the San Andreas fault, *Nature*, *383*, 65–68.

Lisowski, M., and W. H. Prescott (1981), Short-range distance measurements along the San Andreas fault system in central California, 1975 to 1979, *Bull. Seismol. Soc. Am.*, *71*, 1607–1624.

Marone, C., C. Scholz, and R. Bilham (1991), On the mechanics of earthquake afterslip, *J. Geophys. Res.*, *96*, 8441–8452.

McGuire, J., and P. Segall (2003), Imaging of aseismic fault slip transients recorded by dense geodetic networks, *Geophys. J. Inter.*, *155*, 778–788.

Miyazaki, S., J. J. McGuire, and P. Segall (2003), A transient subduction zone slip episode in southwest Japan observed by the nationwide GPS array, *J. Geophys. Res.*, *108*(B2), 2087, doi:10.1029/2001JB000456.

Miyazaki, S., P. Segall, J. Fukuda, and T. Kato (2004), Space time distribution of afterslip following the 2003 Tokachi-oki earthquake: Implications for variations in fault zone frictional properties, *Geophys. Res. Lett.*, *31*, L06623, doi:10.1029/2003GL019410.

Murray, J. R., P. Segall, P. Cervelli, W. Prescott, and J. Svarc (2001), Inversion of GPS data for spatially variable slip-rate on the San Andreas fault near Parkfield, CA, *Geophys. Res. Lett.*, *28*, 359–362.

Nadeau, R. M., and T. V. McEvilly (1999), Fault slip rates at depth from recurrence intervals of repeating microearthquakes, *Science*, *285*, 718–721.

Okada, Y. (1985), Surface deformation due to shear and tensile faults in a half-space, *Bull. Seismol. Soc. Am.*, *75*, 1135–1154.

Okada, Y. (1992), Internal deformation due to shear and tensile faults in a half-space, *Bull. Seismol. Soc. Am.*, *82*, 1018–1040.

Ozawa, S., et al. (2002), Detection and monitoring of ongoing aseismic slip in the Tokai region, central Japan, *Science*, *298*, 1009–1012.

Rauch, H., F. Tung, and C. Striebel (1965), Maximum likelihood estimates of linear dynamic systems, *AIAA J.*, *3*, 1445–1450.

Rice, J., and J.-C. Gu (1983), Earthquake aftereffects and triggered seismic phenomena, *Pure Appl. Geophys.*, *121*, 187–219.

Roeloffs, E. (2001), Creep rate changes at Parkfield, California, 1966–1999: Seasonal, precipitation induced, and tectonic, *J. Geophys. Res.*, *106*, 16,525–16,547.

Rogers, G., and H. Dragert (2003), Episodic tremor and slip on the Cascadia subduction zone: The chatter of silent slip, *Science*, *300*, 1942–1943.

Rymer, M., R. Catchings, M. Thayer, and J. R. Arrowsmith (2004), Structure of the San Andreas fault zone and SAFOD drill site as revealed by surface geologic mapping and seismic profiling near Parkfield, California, *Eos Trans. AGU*, *85*, Fall Meet. Suppl., Abstract T11F-08.

Sammis, C. G., and J. R. Rice (2001), Repeating earthquakes as low-stress-drop events at a border between locked and creeping fault patches, *Bull. Seismol. Soc. Am.*, *91*, 532–537.

Savage, J. C. (1990), Equivalent strike-slip earthquake cycles in half-space and lithosphere-asthenosphere Earth models, *J. Geophys. Res.*, *95*, 4873–4879.

Segall, P., and Y. Du (1993), How similar were the 1934 and 1966 Parkfield earthquakes?, *J. Geophys. Res.*, *98*, 4527–4538.

Segall, P., and M. Matthews (1997), Time dependent inversion of geodetic data, *J. Geophys. Res.*, *102*, 22,391–22,409.

Sims, J. D. (1990), Geologic map of the San Andreas fault in the Parkfield 7.5-minute quadrangle, Monterey and Fresno counties, California, *U.S. Geol. Surv. Misc. Field Stud. Map, MF-2115*.

Waldhauser, F., W. Ellsworth, D. Schaff, and A. Cole (2004), Streaks, multiplets, and holes: High-resolution spatio-temporal behavior of Parkfield seismicity, *Geophys. Res. Lett.*, *31*, L18608, doi:10.1029/2004GL020649.

Yoshioka, S., T. Mikumo, V. Kostoglodov, K. M. Larson, A. R. Lowry, and S. K. Singh (2004), Interplate coupling and a recent aseismic slow slip event in the Guerrero seismic gap of the Mexican subduction zone, as deduced from GPS data inversion using a Bayesian information criterion, *Phys. Earth Planet. Inter.*, *146*, 513–530.

J. R. Murray, U. S. Geological Survey, 345 Middlefield Road, MS 977, Menlo Park, CA 94025, USA. (jrmurray@usgs.gov)

P. Segall, Department of Geophysics, Stanford University, Stanford, CA 94305, USA. (segall@pangea.stanford.edu)